

# Limits on the Peculiar Velocities of Two Distant Clusters Using the Kinematic Sunyaev-Zel'dovich Effect

W.L. Holzapfel<sup>1</sup>, P.A.R. Ade<sup>2</sup>, S.E. Church<sup>3</sup>,  
P.D. Mauskopf<sup>3,4</sup>, Y. Rephaeli<sup>5</sup>, T.M. Willbanks<sup>6</sup> and A.E. Lange<sup>3</sup>

## ABSTRACT

We report millimeter-wavelength observations of the Sunyaev-Zel'dovich (S-Z) effect in two distant galaxy clusters. A relativistically correct analysis of the S-Z data is combined with the results of X-ray observations to determine the radial peculiar velocities ( $v_r$ ) of the clusters. We observed Abell 2163 ( $z = .201$ ) in three mm-wavelength bands centered at 2.1, 1.4, and 1.1 mm. We report a significant detection of the thermal component of the S-Z effect seen as both a decrement in the brightness of the CMB at 2.1 mm, and as an increment at 1.1 mm. Including uncertainties due to the calibration of the instrument, distribution and temperature of the IC gas, and astrophysical confusion, a simultaneous fit to the data in all three bands gives  $v_r = +490_{-880}^{+1370}$  kms<sup>-1</sup> at 68% confidence. We observed Abell 1689 ( $z = .181$ ) in the 2.1 and 1.4 mm bands. Including the same detailed accounting of uncertainty, a simultaneous fit to the data in both bands gives  $v_r = +170_{-630}^{+815}$  kms<sup>-1</sup>. The limits on the peculiar velocities of A2163 and A1689 correspond to deviations from the uniform Hubble flow of  $\lesssim 2 - 3\%$ .

*Subject headings:* cosmology: observations — cosmic microwave background — galaxies: clusters: individual (Abell 2163, Abell 1689) — X-rays: galaxies — large-scale structure of the universe

---

<sup>1</sup>Enrico Fermi Institute, University of Chicago, Chicago IL 60637

<sup>2</sup>Department of Physics, Queen Mary and Westfield College, Mile End Road, London, E1 4NS, U.K.

<sup>3</sup>Department of Physics, Math, and Astronomy, California Institute of Technology, Pasadena CA 91125

<sup>4</sup>Department of Physics, University of California, Berkeley, CA 94720

<sup>5</sup>Center for Particle Astrophysics, University of California, Berkeley, CA 94720

<sup>6</sup>Aradigm Corporation, 26219 Eden Landing Road, Hayward CA 94545

## 1. Introduction

Inhomogeneities in the large-scale mass distribution of the universe produce, through their gravitational interaction, a corresponding velocity field. Measurements of this velocity field can place useful constraints on cosmological models, including the mass density of the universe (e.g., Dekel 1994). Galaxy clusters have been shown to be effective tracers of the large-scale velocity field of the universe (Bahcall *et al.* 1994; Gramann *et al.* 1995). Standard methods for determining the radial peculiar velocities ( $v_r$ ) of clusters difference the velocity determined from the redshift ( $z$ ) with that expected for the uniform Hubble flow,

$$v_r = \frac{c}{q_0} \left[ q_0 z + (q_0 - 1) \left( \sqrt{2q_0 z + 1} - 1 \right) \right] - H_0 d_L, \quad (1)$$

where  $H_0$  is the Hubble constant and  $q_0$  is the deceleration parameter. The luminosity distance to the cluster ( $d_L$ ) is typically determined with an empirical relationship relating the brightness of a standard candle to its distance. In general, the uncertainties in the distance indicators, and therefore, the cluster peculiar velocities, increase linearly with distance.

The interaction of the Cosmic Microwave Background (CMB) with hot intracluster (IC) gas bound to clusters of galaxies provides a method to directly determine the radial peculiar velocities of galaxy clusters. Compton scattering of the CMB by hot IC gas – the Sunyaev-Zel’dovich (S-Z) effect – gives rise to an observable distortion of the CMB spectrum. For a general review of the S-Z effect, see Rephaeli (1995a). The change in CMB intensity caused by the scattering has a thermal component due to the random motions of the scattering electrons (Sunyaev & Zel’dovich 1972), and a kinematic component due to the bulk peculiar velocity of the cluster gas (Sunyaev & Zel’dovich 1980). The S-Z thermal component produces a decrement in CMB intensity at low frequency and an increment at high frequency, while the kinematic component appears as an increment or decrement at all frequencies. In Figure 1, we show the change in the CMB intensity for the two components of the S-Z effect as a function of frequency. Accurate measurements at two or more millimeter/submillimeter wavelengths can, in principle, separate the two components of the S-Z effect.

When combined with X-ray measurements, the amplitude of the thermal component can be used to

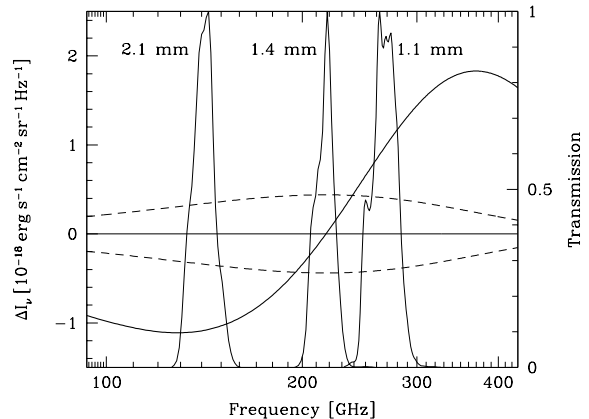


Fig. 1.— Change in CMB Intensity due to the two components of the S- Z effect. The non-relativistic approximation to the thermal component (solid line) is plotted for  $y = 10^{-4}$  and the kinematic component (dashed line) is plotted for ( $v_r = \pm 1000 \text{ km s}^{-1}$ ,  $\tau = 0.01$ ). The average transmissions of the three SuZIE spectral bands (normalized to one) are superimposed.

determine  $H_0$  (Cavaliere *et al.* 1979; Birkinshaw *et al.* 1991). The ratio of the kinematic and thermal component intensities can be combined with the IC gas temperature to determine the radial component of the cluster peculiar velocity (Sunyaev & Zel’dovich 1980; Rephaeli & Lahav 1991). Because the surface brightness of the S-Z effect is independent of redshift and the derived peculiar velocity is weakly dependent on IC gas distribution and temperature, accurate peculiar velocities can be determined for distant clusters which, in general, have poor X-ray data.

We have developed an instrument and observing strategy which achieves high sensitivity to the S-Z effect in three mm-wavelength bands while minimizing systematic errors (Holzapfel *et al.* 1997a). This paper describes the observations and analysis used to place upper limits on the peculiar velocities of two distant galaxy clusters. In Section 2., we discuss the spectra of the S-Z effect and the determination of peculiar velocities. The instrument used to make the S-Z observations and its calibration are described in Section 3.. Analysis of the S-Z data is described in Section 4.. The results of the observations of A2163 and A1689 are described in Sections 5. and 6.. Astrophysical confusion of the S-Z effect, including the con-

tribution of primary CMB anisotropies, is discussed in Section 7.. We summarize our results and conclusions in Section 8..

## 2. Theory

### 2.1. Relativistic Comptonization in Clusters

The Sunyaev & Zel'dovich (1972) treatment of CMB Comptonization, which is commonly used in the analysis of the S-Z effect in clusters, is valid only at low gas temperatures. The determination of accurate cluster peculiar velocities using the S-Z effect requires the use of the relativistically correct treatment of the Comptonization. We express the relativistically correct intensity difference as

$$\Delta I_T = I_0 \int \Psi(x, T_e) d\tau, \quad (2)$$

where  $I_0 = 2(kT_0)^3/(hc)^2$ ,  $T_0$  is the CMB temperature,  $d\tau = n_e \sigma_T dl$ , and the integral is along the line of sight through the cluster. The spectrum is given by

$$\Psi(x, T_e) = \frac{x^3}{(e^x - 1)} [\Phi(x, T_e) - 1], \quad (3)$$

where  $\Phi(x, T_e)$  is a three dimensional integral fully specified in Rephaeli (1995b). To facilitate comparison of our results with low frequency observations, we determine an effective Comptonization in terms of the measured surface brightness,

$$y = \frac{\Delta I_T}{I_0} \left[ \frac{\int \frac{kT_e}{m_e c^2} d\tau}{\int \Psi(x, T_e) d\tau} \right]. \quad (4)$$

As we will demonstrate in Section 3.3.2., neglecting relativistic corrections would lead to considerable errors in the cluster peculiar velocity. All results are calculated using the relativistically correct treatment of the Comptonization unless otherwise stated.

### 2.2. Peculiar Velocity from S-Z and X-Ray Measurements

If the IC gas has a bulk velocity ( $\vec{v}_p$ ) with respect to the CMB frame, there is an additional kinematic component to the S-Z effect,

$$\Delta I_K = -I_0 h(x) \int n_e \sigma_T \frac{\vec{v}_p}{c} \cdot \vec{dl}, \quad (5)$$

where the spectrum is given by  $h(x) = x^4 e^x / (e^x - 1)^2$ , identical to that for a change in the CMB temperature.

Following Birkinshaw, Hughes & Arnaud (1991) (BHA), we express the IC gas temperature and density in terms of the product of a reference value and a dimensionless form factor (BHA equations 3.3 - 3.4):

$$n_e = n_{e0} f_n(\theta, \phi, \xi), \quad (6)$$

$$T_e = T_{e0} f_T(\theta, \phi, \xi). \quad (7)$$

The angle  $\theta$  is measured from a reference line of sight,  $\phi$  is the azimuthal angle about that line of sight, and  $\xi$  is the angular distance along the line of sight. We extend this treatment to include a term describing the temperature dependence of relativistic Comptonization,

$$\Psi(x, T_e) = \Psi_0(x, T_{e0}) f_\Psi[f_T(\theta, \phi, \xi)]. \quad (8)$$

The expressions for the intensity of the S-Z components, equations 2 and 5, then become:

$$\Delta I_T(\theta, \phi) = I_0 n_{e0} \sigma_T d_A \Psi_0(x, T_{e0}) \int d\xi f_n f_\Psi \quad (9)$$

$$\Delta I_K(\theta, \phi) = -I_0 n_{e0} \sigma_T d_A h(x) \frac{v_r}{c} \int d\xi f_n. \quad (10)$$

The structural information for the cluster is contained in the angular form factors:

$$\Theta_T(\theta, \phi) = \int d\xi f_n f_\Psi, \quad (11)$$

$$\Theta_K(\theta, \phi) = \int d\xi f_n. \quad (12)$$

The peculiar velocity can be expressed in terms of the intensity ratio of the two components of the S-Z effect,

$$\frac{v_r}{c} = - \frac{\Delta I_K \Psi_0(x, T_{e0}) \Theta_T(x, T_{e0})}{\Delta I_T h(x) \Theta_K}. \quad (13)$$

In general, measurements are made over finite bands in frequency which contain contributions from both components of the S-Z effect. The intensities of the two components of the S-Z effect can be expressed as linear combinations of the intensities in the measured bands. In the case where the IC gas is isothermal, the angular scale factors  $\Theta_T$  and  $\Theta_K$  are identical and results for  $v_r$  depend only on the ratios of the measured band intensities.

### 3. Observations of the S-Z Effect

#### 3.1. Instrument

The S-Z observations were made using the Sunyaev-Zel'dovich Infrared Experiment (SuZIE) bolometer array at the Caltech Submillimeter Observatory (CSO) on Mauna Kea. A detailed description of the SuZIE instrument has been presented elsewhere (Holzapfel *et al.* 1997a). SuZIE is a  $2 \times 3$  array of 300 mK bolometric detectors optimized for observations of the S-Z effect in distant ( $z > .1$ ) clusters of galaxies. The array consists of two rows separated by  $2.2'$  in declination; each row consists of three co-linear array elements separated by  $2.3'$  in right ascension (RA). Each array element produces a beam on the sky which is approximately  $1.7'$  FWHM.

The spectral responses of the array elements are determined by a common set of metal-mesh filters. The filters can be changed for observations in three mm-wavelength passbands. The 2.1 and 1.1 mm filter passbands are designed to maximize the ratio of the S-Z thermal component signal to the sum of the atmosphere and detector noise. The 1.4 mm filter band is designed to have high sensitivity to the S-Z kinematic component while constraining the net thermal component contribution to be near zero. Due to relativistic corrections, this cannot be done for all IC gas temperatures; in general, the 1.4 mm band contains some residual thermal component signal (see Section 3.3.2.). The average transmission of each of the three SuZIE pass-bands are shown in Figure 1.

Array elements within each of the two rows are electronically differenced by placing pairs of detectors in AC biased bridge circuits. The output of each bridge is synchronously demodulated to produce a stable DC voltage proportional to the instantaneous brightness difference between the two array elements. The bolometer differences strongly reject signals common to both elements, such as fluctuations in the temperature of the 300 mK heat sink and atmospheric emission. Each row provides three differences, two with beam throws of  $2.3'$  and one with  $4.6'$ .

#### 3.2. Scan Strategy

For observations of the S-Z effect, the SuZIE array is used in drift scanning mode. The telescope first tracks a position leading the source by a right ascension offset (RAO). To begin the scan, the telescope stops tracking and is fixed in place; the rotation of

the earth drifts the source across the array of detectors. The scans are roughly  $30'$  in length and last  $\sim 120/(\cos\delta)$  sec for low declination ( $\delta$ ) clusters. Between scans, the array is rotated about the optical axis so that the two rows of the array are kept parallel to the direction of the scan. Keeping the telescope fixed while taking data eliminates signals due to modulation of the telescope's side-lobes and microphonic response of the detectors. After a scan, the telescope tracks a new position leading the source by a different RAO and a new scan is begun. This cycle, which alternates the RAO between scans is repeated indefinitely. In Section 4.6., we use the alternation of the RAO between scans to test for an instrumental baseline.

#### 3.3. Calibration

##### 3.3.1. Flux Calibration

Observations of planets are used to map the beam shapes of the instrument and calibrate the responsivity of the detector elements. In April 1993 and 1994, Uranus was used to calibrate the 2.1 mm observations. We used scans of Uranus to calibrate the 1.4 mm band in May 1994. In May 1993, observations of Mars were used to calibrate 1.1 mm band observations. Rotation of the array about the optical axis results in small reproducible changes in the instrument's beam-shapes. For each band, we mapped the beam shapes over the range of dewar rotation angles for which we observed the source; the calibrations computed for the range of rotation angles at which we observed the sources change by less than 5%.

The brightness of Uranus is found from a third order polynomial fit to the measured brightness temperature as a function of wavelength (Griffin and Orton 1993). The brightness temperature of Mars is taken from Orton *et al.* (1986). The authors assign  $\pm 6\%$  uncertainty to the brightness of Uranus, most of which arises from the  $\pm 5\%$  uncertainty in the absolute brightness of Mars from which Uranus is calibrated. Combining the uncertainties in the measured beam-shapes and absolute brightness of the planetary calibrator, the uncertainty in the calibration of the instrument to surface brightness in each of the spectral bands, is estimated to be  $\sim \pm 8\%$ .

We use these results to calculate the contribution of the uncertainty in flux calibration to the uncertainty in the peculiar velocity determined from measurements in two spectral bands. Because the pe-

cular velocity can be expressed as a ratio of measured brightnesses, a calibration error which is common across the bands, such as the uncertainty in the absolute calibration of the planetary calibrator is likely to contribute, makes no contribution to the uncertainty. We have calculated the flux calibration error assuming the worst (and unlikely) case that the  $< 5\%$  uncertainty in the measured beam-shapes is anticorrelated between bands. For the combination of the 2.1 and 1.1 mm data, we determine the contribution to the uncertainty in the peculiar velocity to be  $\Delta v_r \lesssim \pm 140(kT_e/10 \text{ keV}) \text{ kms}^{-1}$ . For the combination of the 2.1 and 1.4 mm data, the contribution to the uncertainty is  $\Delta v_r \lesssim \pm 6(kT_e/10 \text{ keV}) \text{ kms}^{-1}$ . The comparatively large uncertainty determined for the 2.1 and 1.1 mm data is because, to determine  $v_r$ , we are (in effect) differencing two large thermal component signals, each with a proportional flux calibration uncertainty. For the combination of the 2.1 and 1.4 mm data, the uncertainty is roughly proportional to the small signal in the 1.4 mm band. For a peculiar velocity determination using the 2.1, 1.4, and 1.1 mm bands, the uncertainty in the flux calibration contributes an uncertainty  $\Delta v_r \sim \pm(6 - 140)(T_e/10 \text{ keV}) \text{ kms}^{-1}$ , depending on the relative significance of the data in the three bands. In our accounting of the uncertainties we assume the worst case, and use the upper limit. In this analysis, we have assumed that 5% of  $v_r$  is a negligible contribution to the total uncertainty, true for the results of this work.

### 3.3.2. Spectral Calibration

The spectral responses of the array elements, including detailed checks for out of band leaks, are measured using a Fourier transform spectrometer. Because the beams of the array look through different portions of the filter at different angles, there are slight differences between their spectral bands. Small deviations of the 1.4 mm band from the null frequency of the thermal effect produce large offsets in the derived peculiar velocities. To demonstrate the size of this effect, we calculate the peculiar velocity that one would determine by assuming all the signal in the 1.4 mm band is due to the kinematic effect,

$$\frac{\Delta v_r}{c} = \frac{\int d\nu \Psi(\nu, T_e) f(\nu)}{\int d\nu h(\nu) f(\nu)}. \quad (14)$$

In the non-relativistic approximation, the thermal effect signal in the average 1.4 mm band is nearly zero.

In Table 1, the scatter of the non-relativistic results about zero are due to the array element differences. The results are listed for  $T_e = 10 \text{ keV}$ ; the offsets scale linearly with the assumed  $T_e$ . These significant differences in the spectral response of the array elements are taken into account by individually calibrating each of them to the two components of the S-Z effect.

Relativistic corrections to the S-Z spectrum lead to significant thermal component signal in the 1.4 mm band. In Table 1, we show the error in peculiar velocity that would be incurred by ignoring relativistic corrections to the S-Z effect for the three principal gas temperatures considered in this work. In the non-relativistic approximation, the average 1.4 mm band is centered at the null of the S-Z thermal effect. Relativistic corrections shift the null to higher frequencies; the change in frequency is linearly dependent on the IC gas temperature (Rephaeli 1995a). The S-Z spectra, as sampled by the narrow 1.4 mm band (See Figure 1), increases nearly linearly with frequency. The amplitude of the thermal component also increases nearly linearly with increasing IC gas temperature. Combining these effects, we find that neglecting relativistic corrections leads to an error in the peculiar velocity determined from the average 1.4 mm band of  $\Delta v_r \approx +360(kT_e/10 \text{ keV})^2$ . This is corrected for by calibrating with the correct relativistic spectra.

There is uncertainty in the results of the laboratory spectroscopy. From repeated spectroscopy runs, we conservatively estimate the uncertainty in the array element central frequencies to be  $< \pm 1\%$ . When the peculiar velocity is determined from the combination of the 2.1 and 1.1 mm band data, the uncertainty in  $v_r$  is  $\pm 137(kT_e/10 \text{ keV}) \text{ kms}^{-1}$ . The steeper slope of the thermal spectra near the null leads to a slightly larger uncertainty of  $\pm 196(kT_e/10 \text{ keV}) \text{ kms}^{-1}$  when the velocity is determined from combination of the 2.1 and 1.4 mm bands. All three bands are used to determine the peculiar velocity of A2163; we conservatively adopt the larger of the uncertainties determined from two bands.

## 4. S-Z Data Analysis

This section describes the reduction and analysis of the S-Z scans. The analysis of the A2163 2.1 mm data set is presented in detail in H97b. The initial reduction of all the S-Z data is identical to that treatment. We outline the analysis method, with particular em-

Thermal Effect Signal in 1.4 mm Band [kms <sup>-1</sup> ]				
Detector	$T_e$ [keV]			non-relativistic (10 keV)
	8.2	12.4	13.3	
1	229	517	581	-25.8
2	399	764	837	210.1
3	299	616	687	72.7
4	113	351	406	-186.0
5	356	702	773	151.5
6	161	420	478	-119.5
average	261	550	627	19.6

Table 1: Residual thermal effect signal in the 1.4 mm band calibrated in terms of an “offset” in peculiar velocity. Results are shown for the three principal IC gas temperatures discussed in this paper. We also show the results using the non-relativistic S-Z spectra for 10 keV IC gas.

phasis on the determination of accurate confidence intervals from multiparameter fits to the S-Z scans.

#### 4.1. Data Set

Each of the two rows of the SuZIE array consists of three detectors;  $s_1$ ,  $s_2$  and  $s_3$ . Detector signals are differenced in pairs (in hardware) to form three difference signals;  $d_{12} = s_1 - s_2$ ,  $d_{23} = s_2 - s_3$ , and  $d_{31} = s_3 - s_1$ . These differences correspond to angular chops of 2.3', 2.3', and 4.6' respectively. The two 2.3' differences are differenced to form a triple beam chop (TBC), for example,

$$t_{123} = d_{12} - d_{23} = s_1 - 2s_2 + s_3. \quad (15)$$

The data set consists of 4 difference signals:  $d_{31}$ ,  $t_{123}$ ,  $d_{64}$ , and  $t_{456}$  corresponding to the 4.6' difference and TBC for each of the two rows of detectors. We refer to these four difference signals as  $d_k$ , where  $k$  ranges from 1 to 4. We also compute the average signal of the undifferenced detectors,

$$s = \frac{1}{6} \sum_k^6 s_k. \quad (16)$$

The average single detector signal is used as a monitor of the absolute atmospheric emission and to remove any residual common mode response from the detector differences.

We clean the raw data of transients due to the interaction of cosmic rays with the detectors. Less than 5% of the data are identified as contaminated by cosmic rays. The raw data are binned into 3 s bins

corresponding to 15 5 Hz samples or  $0.75' \cos(\delta)$  on the sky. Samples flagged as bad due to cosmic rays are left out when the bin averages are computed; bins with more than half of their samples flagged are not used in the analysis. For each scan  $j$ , and bin  $i$ , the binned differential and average single detector signals are expressed as  $d_{kji}$  and  $s_{ji}$ .

#### 4.2. S-Z Surface Brightness Model

The S-Z surface brightness profile of A2163 has a FWHM  $\approx 5'$ , which is comparable to the largest beam-throw of SuZIE. In order to accurately determine the peak surface brightness, we must simulate the observation of the extended source. Models for the surface brightness of the S-Z thermal and kinematic components are constructed from the X-ray surface brightness determined density profile and the assumption of some thermal structure. We express the surface brightness morphology in terms of dimensionless form factors normalized to one at peak brightness:

$$S_{T_i}(\theta, \phi) = \frac{\Delta I_{T\nu_i}(\theta, \phi)}{\Delta I_{T\nu_i}(0, 0)} = \frac{\int f_n(\theta, \phi, \xi) f_{\Psi_i}(\theta, \phi, \xi) d\xi}{\int f_n(0, 0, \xi) f_{\Psi_i}(0, 0, \xi) d\xi}, \quad (17)$$

$$S_{K_i}(\theta, \phi) = \frac{\Delta I_{K\nu_i}(\theta, \phi)}{\Delta I_{K\nu_i}(0, 0)} = \frac{\int f_n(\theta, \phi, \xi) d\xi}{\int f_n(0, 0, \xi) d\xi}. \quad (18)$$

To take differences in the array elements into account,  $S_{K,T_i}$  are evaluated at the S-Z intensity weighted band center for each array element  $i$ . In the case of an isothermal IC gas,  $S_{T_i}(\theta, \phi) = S_{K_i}(\theta, \phi)$  for all  $i$ .

The form factor for the desired S-Z component ( $S_{K,T_i}$ ) is convolved with beam-maps constructed

from the voltage response of the detectors to scans over planets,  $V_{Pi}$ . This forms a template for the response of each detector to the assumed surface brightness of the S-Z components,

$$sm_{K,Ti}(\theta) = \frac{\Delta I_{K,Ti}}{I_{Pi}} \frac{1}{\Omega_P} \int V_{Pi}(\theta - \theta', \phi') S_{K,T}(\theta', \phi') d\theta' d\phi', \quad (19)$$

where  $\Omega_P$  is the solid angle subtended by the planetary calibrator. This expression assumes the planetary calibrator to be much smaller than the beams on the sky, true for Mars and Uranus. To calibrate the model, we determine the ratio of the relativistically correct S-Z brightness to the brightness of the planet,

$$\frac{I_{K,Ti}}{I_{Pi}} = \frac{\int f_i(\nu) I_{K,T\nu} d\nu}{\int f_i(\nu) I_{P\nu} d\nu}, \quad (20)$$

where  $f_i(\nu)$  is the measured spectral response and  $I_{P\nu}$  is the intensity of the planetary calibrator. The S-Z brightness is calculated for  $y = 1$  and  $v_r = 1 \text{ km s}^{-1}$ , so the results of the model fits are in convenient units.

The models for the response of the single array elements are differenced to create models for the response of the detector differences. The  $\sim .05'$  resolution differential source models are binned identically to the scan data to determine the model signal for each of the  $\sim .75'$  data bins. The binned differential models are designated as  $m_{ki}(RA)$ , where  $k$  is one of the four detector differences,  $i$  is the position (by bin number) in the scan, and RA is a offset of the model from the nominal X-ray determined position.

### 4.3. Coadded Data

We coadd the difference signals to create high sensitivity scans of the differential surface brightness as a function of RA. For each difference channel  $k$ , and scan  $j$ , we clean the data by removing the best fit linear baseline and residual common-mode signal ( $\alpha_{kj} s_{ji}$ ),

$$x_{kji} = d_{kji} - \alpha_{kj} s_{ji} - a_{kj} - i b_{kj}. \quad (21)$$

The residual common-mode signal is the small signal in the detector differences that is correlated with the average single detector signal. Removing this signal improves the rejection of the differential signals to common mode atmospheric noise. In H97b, we show that removing it has no systematic effect on the fit results.

The value of each coadded bin  $x_{ki}$ , is given by the weighted sum of the value of this bin in each of  $N_s$  scans,

$$x_{ki} = \frac{\sum_{j=1}^{N_s} \frac{x_{kji}}{RMS_{kj}^2}}{\sum_{j=1}^{N_s} \frac{1}{RMS_{kj}^2}}. \quad (22)$$

Each bin is weighted by the residual RMS of the scan,

$$RMS_{kj}^2 = \frac{\sum_{i=1}^{N_b} x_{kji}^2}{(N_b - 1)}, \quad (23)$$

where  $N_b$  is the number of bins in a scan. The uncertainty in the value of each bin is determined from the weighted dispersion of the value of that bin about the mean determined from  $N_s$  scans,

$$\sigma_{ki} = \sqrt{\frac{\sum_{j=1}^{N_s} \frac{(x_{ki} - x_{kji})^2}{RMS_{kj}^2}}{(N_s - 1) \sum_{j=1}^{N_s} \frac{1}{RMS_{kj}^2}}}. \quad (24)$$

The best fit peak Comptonization ( $y_0$ ) and isothermal model position ( $RA$ ) are found by minimizing the  $\chi^2$  of the fit to all four difference signals for each of the coadded 2.1 mm data sets,

$$\chi^2 = \sum_{k=1}^4 \sum_{i=1}^{N_b} \frac{(x_{ki} - y_0 m_{Tki}(RA) - a_k - i b_k)^2}{\sigma_{ki}^2}. \quad (25)$$

The linear baseline is unconstrained to make sure that our removal of a linear baseline in equation 21 did not effect the signal. For each value of RA, we re-bin the  $.05'$  resolution source model to determine the model signal for each of the  $\sim .75'$  data bins.

If the source contributes significantly in a single scan, then a scan in which the noise and source conspire to produce a low RMS and corresponding low signal will be weighted higher. Coadding the scans using equations 21–23 could introduce a bias in the amplitude of the coadded scans. In H97b, we eliminate this bias by recomputing the coadded bins with each bin weighted on the residual RMS with the average source model removed. We do this for all the coadded data presented in this paper as well, although it is unlikely to be necessary for the extremely low signal to noise 1.4 and 1.1 mm scans.

#### 4.4. Single scan fits

The determination of accurate uncertainties for fits to the coadded scans is difficult due to the presence of atmospheric noise which is correlated between bins and detector differences. Ignoring this correlation leads to a significant overestimate of the significance of the fit results. In this section, we use the distribution of the single scan fit amplitudes to determine accurate uncertainties for model amplitudes. These results are then used to correct the error in the coadded fit uncertainties due to correlated sky noise.

The noise in scans taken at different times is uncorrelated. Each scan can be treated as an independent measurement of the source amplitude. We determine the mean single-scan peak Comptonization for a given observation by averaging the values  $y_{0j}$  for each of the  $N_s$  scans,

$$y_0 = \frac{\sum_{j=1}^{N_s} \frac{y_{0j}}{\sigma_{yj}^2}}{\sum_{j=1}^{N_s} \frac{1}{\sigma_{yj}^2}}, \quad (26)$$

where  $\sigma_{yj}$  is the change in  $y_{0j}$  corresponding to  $\Delta\chi^2 = 1$  in the model fit. The weighted dispersion of the scan amplitudes about the mean is used to estimate the uncertainty in the determination of the mean,

$$\sigma_y = \sqrt{\frac{\sum_{j=1}^{N_s} \frac{(y_0 - y_{0j})^2}{\sigma_{yj}^2}}{(N_s - 1) \sum_{j=1}^{N_s} \frac{1}{\sigma_{yj}^2}}}. \quad (27)$$

In H97b, we plot the distribution of single scan fit amplitudes for all of the 2.1 mm scans across A2163. As in that example, the distribution of scan fit amplitudes for all the data sets considered here are well approximated by a Gaussian. The width of the distribution is a function of the amount of sky noise and is correlated with the RMS of the scans. Using the weighting scheme described in this section, we narrow the distribution slightly by decreasing the weight of the scans with large sky noise.

#### 4.5. Confidence intervals

From the single-scan fits we have an accurate measurement of the uncertainty in the source amplitude for each data set,  $\sigma_y$ . We compare this to the uncertainty ( $\sigma_{yca}$ ) determined from the fits to the coadded data (equation 25;  $\Delta\chi^2 = 1$ ). We compute a scaling

factor to correct for the underestimation of the bin uncertainties for each data set,  $m$ .

$$\gamma_m = \frac{\sigma_y}{\sigma_{yca}}. \quad (28)$$

Depending on the details of the atmosphere at the time of the measurement,  $\gamma_m = 1.4 - 2.0$ . Each coadded scan is individually scaled so that the uncertainties in the coadded scan fit amplitudes are equal to the single-scan fit uncertainties. Fits to the coadded data (for similar model shapes and positions) will then result in accurate uncertainties for the fit parameters. Essentially, we have reduced the number of degrees of freedom to account for the correlated noise. The resulting confidence intervals are a factor of 1.4 to 2.0 larger than those found from the uncorrected data. All confidence intervals in this paper are computed using coadded data that has been corrected for correlated sky noise in this way.

We determine confidence intervals for the source position, peculiar velocity, peak Comptonization and isothermal  $\beta$  model parameters using a maximum likelihood estimator,

$$L_m(\zeta) = \prod_{k=1}^4 \prod_{i=1}^N \frac{1}{(2\pi \gamma_m \sigma_{ki})^{1/2}} \exp \left[ \frac{-\zeta_{ki}^2(y, z)}{2(\gamma_m \sigma_{ki})^2} \right], \quad (29)$$

where  $\zeta_k = x_{ki} - y_0 m_{Tki}(RA, \theta_c, \beta) - v_r m_{Kki}(RA, \theta, \beta) - a_k - i b_k$  is the coadded scan with the kinematic and thermal component source models removed. The coadded scans corresponding to different RAOs and frequency bands are treated as independent; the likelihood for simultaneous fits of  $k$  scans for each of  $m$  uncorrelated data sets is given by,

$$L(\zeta) = \prod_m \prod_k L_{mk}(\zeta). \quad (30)$$

To make the problem computationally tractable we determine the likelihood for only two interesting parameters at a time. The likelihoods are determined for a necessarily large grid in the parameter space with resolution:  $\Delta RA = .05'$ ,  $\Delta v_r = 10 \text{ kms}^{-1}$ , and  $\Delta y_0 = 2 \times 10^{-6}$ . Assuming no peculiar velocity, fits to the X-ray derived isothermal thermal component model determine the source position and amplitude. The resulting position is insensitive to the values of the peculiar velocity and  $\beta$  model parameters. For the rest of the analysis, we fix the source position to its best fit value. The isothermal  $\beta$  model parameters

are determined with the source amplitude free to vary. We do this to check that the assumed model is consistent with the S-Z data. Finally, we fix the position and  $\beta$  parameters for the the thermal and kinematic component models and determine the likelihood for  $v_r$  and  $y_0$ .

The likelihood grids are converted to confidence regions and intervals in the interesting parameters. Invoking Bayes' theorem and assuming a uniform prior, the probability that the two fit parameters  $(y, z)$  fall within a region  $R$  is given by

$$P(R) = \frac{\int \int_R L(y, z) dydz}{\int_{-\infty}^{\infty} \int_{-\infty}^{\infty} L(y, z) dydz}. \quad (31)$$

The confidence interval corresponding to a probability  $P_0$  is given by the region  $R_0$  such that  $P(R_0) = P_0$  and  $L[(y, z) \in R_0] \geq L[(y, z) \notin R_0]$ . We determine the likelihood in a single parameter by marginalizing the likelihood over the uninteresting parameters,

$$L(z) = \int_{-\infty}^{\infty} L(y, z) dy. \quad (32)$$

The probability that the parameter  $y$  falls within the interval  $I = [z_1, z_2]$  is given by,

$$P(I) = \frac{\int_I L(z) dz}{\int_{-\infty}^{\infty} L(z) dz}. \quad (33)$$

The confidence interval corresponding to a probability  $P_0$  is given by  $I_0 = [z_1, z_2]$  such that  $P(I_0) = P_0$  and  $L(z \in I_0) \geq L(z \notin I_0)$ . All the 68% confidence levels quoted in Sections 5. and 6. are calculated this way unless otherwise stated.

#### 4.6. Baseline

We have carefully designed our instrument and scan strategy to eliminate systematic errors. However, it is possible that the instrument could introduce some systematic signal similar to the expected cluster signal. To test for the presence of this type of instrumental baseline, we gather “blank sky” scans across regions of sky free of known sources. These data are analyzed exactly as the source data; the presence of an instrumental baseline would result in the determination of a non-zero signal for these regions.

In April 1994, we accumulated  $\sim 15$  hours of 2.1 mm data on two patches of sky free of known sources. The analysis of these data are described in Holzapfel *et al.* (1997b). Fitting these data to

the isothermal thermal effect model for A2163 with the position in the scan fixed at the best fit position from the source observations, we determine  $y_0 = 1.55 \pm 2.13 \times 10^{-5}$ . In May 1993, we accumulated  $\sim 7.2$  hours of 1.1 mm data on three patches of sky free of known sources. Fitting these data to the isothermal thermal effect model for A2163, we determine  $y_0 = -.21 \pm 2.17 \times 10^{-4}$ . In May 1994, we accumulated  $\sim 16.3$  hours of 1.4 mm data on two patches of sky free of known sources. Fitting these data to the kinematic component source model for A2163 and assuming  $\tau = .015$ , we find  $v_r = +760 \pm 1050 \text{ kms}^{-1}$ . Therefore, we detect no significant baseline in any of the three spectral bands.

We could subtract these scans from the source scans to remove a possible instrumental baseline. Unfortunately, due to shorter integrations and poorer weather, the “blank sky” data in the 1.4 and 1.1 mm bands is less sensitive than the source data; the subtraction of these scans would significantly increase the uncertainty in the fit results. Another problem with this procedure is that the baseline and source data, although gathered at similar azimuth and zenith angle, are gathered at different times. Any baseline signal, because it is not significant in a single scan, must be correlated in time between several scans. However, this does not guarantee an instrumental baseline will be constant over the course of the night.

We have devised an observation strategy which allows us to check for, and remove, any time correlated baseline. Differencing scans taken adjacent in time at two different RAOs allows the subtraction of any common baseline while retaining most of the expected source signal. Each pair of scans are differenced by subtracting their raw 5 Hz sampled time streams. The data are then analyzed exactly as described in Sections 4.-4.5..

We construct a model for the RAO differenced surface brightness by subtracting two models with the appropriate RAO difference between them. We chose the RAO difference ( $\delta'$ ) to be large enough so that (for most clusters) the two models have little overlap in time and therefore will not subtract much signal when differenced. The RAO differenced model is fit to the RAO differenced data to determine the source amplitude and position. In all cases the results agree, within the quoted statistical error, with those found from fits to both RAOs. The lack of any significant change when the scans are differenced indicates that there is no significant instrumental baseline in

the data. We use the difference between the results of the RA differenced and standard analysis as an estimate of the uncertainty due to the possibility of an instrumental baseline.

## 5. A2163

### 5.1. X-ray Surface Brightness

Abell 2163 is a distant ( $z = .201$ ) X-ray luminous cluster of galaxies with the distinction of having the highest X-ray temperature of any cluster yet observed. A2163 was the target of pointed observations by the GINGA, ROSAT and ASCA satellites. A detailed analysis of each of these observations has been published (Arnaud *et al.* 1992; Elbaz *et al.* 1994; Markevitch *et al.* 1996). The ROSAT/PSPC was used to determine the spatial dependence of the X-ray surface brightness. The peak surface brightness was found at  $16^{\text{h}} 15^{\text{m}} 46^{\text{s}}$ ;  $-06^{\circ} 09' 02''$  (J2000). The radial profile was determined by summing annuli about this position, with significant emission detected up to  $18'$  from the position of the peak. Assuming the IC gas to be isothermal, the surface brightness profile was fit with the combination of an isothermal  $\beta$  model and a constant background. The density profiles are assumed to have the form of a spherically symmetric  $\beta$  model,

$$f_n(\theta, \phi, \xi) = \left[ 1 + \left( \frac{\theta^2 + \phi^2 + \xi^2}{\theta_c^2} \right) \right]^{-\frac{3}{2}\beta}. \quad (34)$$

The best fit model parameters were found to be  $\beta = .616_{-.009}^{+.012}$  and  $\theta_c = 1.20 \pm 0.05'$  at 68.3% confidence (Elbaz *et al.* 1994).

### 5.2. Thermal Structure

In H97b, the thermal structure of the IC gas in A2163 is discussed in detail, here we summarize only the essential points. A combined analysis of the ASCA/GIS+SIS and GINGA spectral data gives temperatures: 13.3, 13.3, and 3.8 keV in three radial bins of 0 – 3, 3 – 6, and 6 – 13 X-ray core radii (Markevitch *et al.* 1996). We use a simple two parameter model to describe the measured temperature profile of A2163. The model consists of an isothermal central region extending to  $\theta_{iso}$  beyond which the temperature decreases according to a polytropic model with

index  $\gamma$ ,

$$T_e(\theta) = \begin{cases} T_{iso} & \theta \leq \theta_{iso} \\ T_{iso} \left[ \frac{1+(\theta/\theta_c)^2}{1+(\theta_{iso}/\theta_c)^2} \right]^{-\frac{3}{2}\beta(\gamma-1)} & \theta > \theta_{iso}. \end{cases} \quad (35)$$

The central temperature is  $T_{e0} \approx 13.3_{-1.8}^{+2.8}$  keV, where the error bars enclose the 68% confidence intervals for both the GINGA and ASCA results, each analyzed independently under the assumption of the ASCA thermal structure (H97b). We adopt thermal model parameters  $\theta_{iso} = 4.0\theta_c$  and  $\gamma = 2.0$  and reanalyze the X-ray data to determine consistent density model parameters  $\beta = .64$  and  $\theta_{iso} = 1.26$ . These results are used to create a model for the thermal component surface brightness that includes the thermal structure.

In the case when the IC gas is assumed to be isothermal, we adopt a temperature which is the emission-weighted average temperature of the above results. For an isothermal IC gas,  $\bar{T}_e \approx 12.4_{-1.7}^{+2.7}$  keV, where the error bars enclose the 68% confidence intervals for both the GINGA and ASCA results, each independently analyzed assuming an isothermal IC gas. The results in this section are for fits to the isothermal source model unless otherwise stated.

### 5.3. 2.1 mm Observations

We have observed A2163 at 2.1 mm in two periods; April 23-26 1993 for a total of 16 hours and April 4, 9, 10, and 11 for 8 hours. The analysis of these data to determine the Hubble constant is presented in Holzzapfel *et al.* (1997b).

The data corresponding to each observation run and RAO are combined to make coadded scans. In Figure 2, we plot the April 1994 coadded 4.6' and TBC scans over A2163 with the best fit isothermal model overlaid. Assuming the peculiar velocity to be zero, the coadded data scans are simultaneously fit to the corresponding isothermal source models with the peak S-Z surface brightness position and peak Comptonization free to vary. In Figure 3, we show the 68.3 and 95.4% confidence regions for the source position and amplitude ( $RA$  and  $y_0$ ). The 68.3% confidence limits for the fit parameters considered individually are  $\Delta RA = .35 \pm .14'$  and  $y_0 = 3.73 \pm 0.35 \times 10^{-4}$ . Including the uncertainties in the ROSAT/PSPC and SuZIE pointing, the positions of the peak X-ray and S-Z surface brightnesses are consistent (Holzapfel *et al.* 1997b).

Fixing the position to the best fit value, we fit

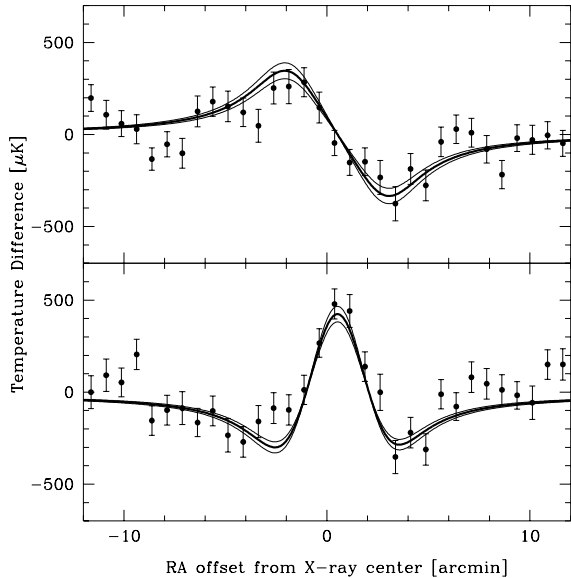


Fig. 2.— Coadded data for all April 1994 scans across A2163 at 2.1 mm. The coadded scans from the two RAOs have been offset and added to create a single coadded scan for each difference. Both the 4.6' difference (upper panel) and TBC (lower panel) data are shown for the row passing directly over the peak X-ray surface brightness. The heavy line is the best fit isothermal model, and the lighter lines represent the  $1\sigma$  errors. The scans are calibrated in terms of a Rayleigh-Jeans temperature difference that completely fills one of the beams.

isothermal  $\beta$  models for the surface brightness distribution to the coadded scans. In Figure 4, we plot approximate confidence regions in  $\theta_c$  and  $\beta$ . Technically, the data lack sufficient sensitivity to determine proper confidence regions in position and amplitude; we approximate the 68.3 and 95.4% confidence regions as corresponding to  $\Delta\chi^2 = 2.3$  and 6.17 respectively. The results of the S-Z fits are consistent with those of the X-ray derived density parameters and an isothermal IC gas. In H97b, we found that the S-Z data did not have sufficient sensitivity to discriminate between an isothermal IC gas and the thermal structure measured with ASCA.

#### 5.4. 1.1 mm Observations

We observed A2163 on May 1-4 1993 for a total of 19.7 hours. Scans were 30' long with one row pass-

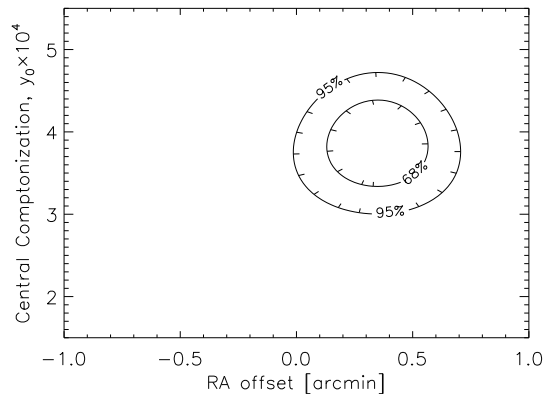


Fig. 3.— Isothermal thermal component model fit to the coadded 2.1 mm data for A2163. Assuming no peculiar velocity, the contours enclose the approximate 68.3% and 95.4% confidence regions in peak Comptonization and RA offset from the X-ray center.

ing over the X-ray center and the other 2.2' to the south. The RAO of the X-ray center from the start of the scan was alternated between 12.5' and 18.5' in sequential scans. The 1.1 mm observations are dominated by sky noise and the quality of the data varies greatly with atmospheric conditions.

In Figure 5, we show the coadded 4.6' and TBC scans over A2163 with the best fit isothermal model overlaid. Assuming the peculiar velocity to be zero, the coadded data scans are simultaneously fit to the corresponding isothermal source model with the position and peak Comptonization free to vary. In Figure 6, we show the approximate confidence regions in RA and  $y_0$  computed for the fits of the isothermal source model to the 1.1 mm coadded data. The approximate single-parameter 68.3% ( $\Delta\chi^2 = 1.0$ ) confidence intervals are  $\Delta RA = .17 \pm .59'$  and  $y_0 = 4.05 \pm 1.47 \times 10^{-4}$ . Both the amplitude and position of the peak S-Z surface brightness are consistent with the results of the 2.1 mm analysis.

#### 5.5. 1.4 mm Observations

We observed A2163 in the 1.4 mm band on the nights of May 5, 6, 7, and 8 1994 for a total of  $\sim 12.3$  hours. Scans were 30' long with one row passing over the X-ray center and the other 2.2' to the south. The RAO of the X-ray center from the start of the scan was alternated between 12' and 18' in se-

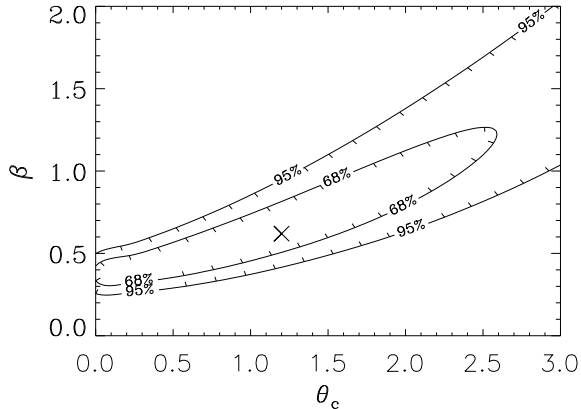


Fig. 4.— Isothermal density model parameter fits to the coadded data scans across A2163. Contours for  $\theta_c$  and  $\beta$  are shown at approximately 68% and 95% confidence. The “X” marks the best fit isothermal model parameter values from the X-ray analysis.

quential scans. In Figure 7, we show the coadded 4.6’ and TBC scans. Fitting the data with a model for the kinematic component, we determine a marginally significant signal, the bulk of which is due to the residual thermal component signal in the 1.4 mm band.

## 5.6. Simultaneous Fits

### 5.6.1. 2 Band Fits

We simultaneously fit the 2.1 and 1.1 mm coadded scans with the S-Z thermal and kinematic component isothermal models generated for each of the two bands. The models are fixed to the best fit position from the 2.1 mm scans. We determine  $v_r = -120_{-1060}^{+1350}$   $\text{kms}^{-1}$  and  $y_0 = 3.92 \pm .59 \times 10^{-4}$  at 68.3% confidence.

We also simultaneously fit the 2.1 and 1.4 mm coadded scans with the S-Z thermal and kinematic component isothermal models generated for each of the two bands. The models are fixed to the best fit position from the 2.1 mm scans. We determine  $v_r = +990_{-1190}^{+1730}$   $\text{kms}^{-1}$  and  $y_0 = 3.45 \pm .63 \times 10^{-4}$  at 68.3% confidence.

### 5.6.2. 2.1 mm, 1.4 mm and 1.1 mm Bands

We simultaneously fit isothermal ( $T_e = 12.4$  keV) models for the kinematic and thermal components of the S-Z effect to the 2.1, 1.4 and 1.1 mm coadded

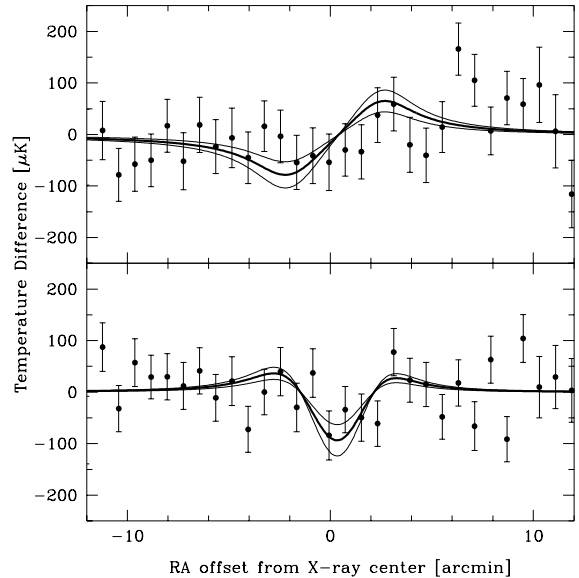


Fig. 5.— Coadded data for all May 1993 scans across A2163 at 1.1 mm. The scans for the two RAOs have been offset and added to create a single coadded scan for each difference. Both the 4.6’ difference (upper panel) and TBC (lower panel) shown for the row passing directly over the peak X-ray surface brightness. The heavy line is the best fit isothermal model, and the lighter lines represent the  $1\sigma$  errors. The scans are calibrated in terms of a Rayleigh-Jeans temperature difference that completely fills one of the beams.

scans. The model positions are fixed to the best fit positions from the 2.1 mm fits; the model amplitudes,  $y_0$  and  $v_r$ , are left as free parameters. We plot the 68.3% and 95.4% confidence regions for  $y_0$  and  $v_r$  in Figure 8. The 68.3% confidence intervals for the fit parameters considered individually are  $v_r = +490_{-730}^{+910}$   $\text{kms}^{-1}$  and  $y_0 = 3.62 \pm .48 \times 10^{-4}$ .

We have repeated this analysis for the range of allowed density models; the results are unchanged within the precision of the grid in  $v_r$  ( $10 \text{ kms}^{-1}$ ). This analysis is repeated using the RAO differenced scans; we compare the results of the two analysis methods in Table 2. The sensitivity in  $v_r$  is much worse for the RAO differenced data. This is due to the large extent of the A2163 surface brightness. A larger RAO difference would reduce the amount of subtracted signal and increase the sensitivity of the RAO differenced data.

Peculiar Velocities: Standard and RAO Differenced

Cluster	Thermal Structure	$kT_{e0}$ [keV]	analysis	$y_0 \times 10^4$	$v_r$ [kms $^{-1}$ ]
A2163	Isothermal	12.4	Both RAOs	$3.62 \pm .49$	$+490_{-730}^{+910}$
A2163	Isothermal	12.4	Differenced	$3.44 \pm .72$	$+1390_{-1440}^{+2350}$
A2163	ASCA	13.3	Both RAOs	$2.96 \pm .39$	$+560_{-800}^{+960}$
A2163	ASCA	13.3	Differenced	$2.34 \pm .57$	$+1460_{-1520}^{+2420}$
A1689	Isothermal	8.2	Both RAOs	$3.43 \pm .59$	$+170_{-570}^{+760}$
A1689	Isothermal	8.2	Differenced	$3.00 \pm .73$	$+310_{-700}^{+1050}$

Table 2: Comparison of peculiar velocities determined with the standard analysis and fits to the RAO differenced scans. All results are at 68% confidence. The differences between the results represent our best limits on possible contribution due to an instrumental baseline. The sensitivity is considerably worse for the RAO differenced scans, especially for A2163, which is more extended than A1689 and has more signal subtracted in the differencing.

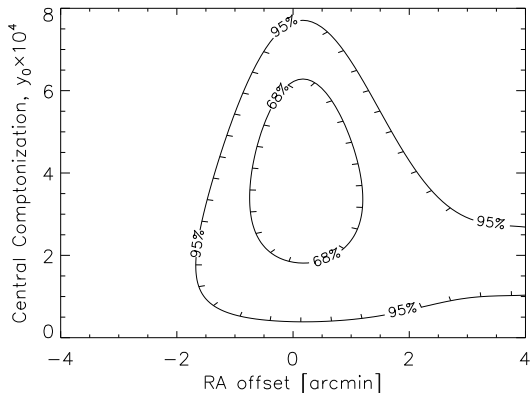


Fig. 6.— Isothermal thermal component model model fit to the coadded 1.1 mm data for A2163. Assuming no peculiar velocity, the contours enclose the approximate 68.3% and 95.4% confidence regions in peak Comptonization and RA offset from the X-ray center (Note: scale is different than Figure 3).

We have repeated the determination of  $v_r$  assuming two other values for the isothermal IC gas temperature which roughly span the 68.3% confidence interval for  $T_e$ . The peculiar velocities determined assuming  $T_e = 10$  and 15 keV are listed in Table 3. The effects of the implied change in optical depth and relativis-

tic corrects cancel. The contribution of the uncertainty in the IC gas temperature to the uncertainty in peculiar velocity ( $\Delta v_r < \pm 20$  kms $^{-1}$ ) is negligible compared to the statistical uncertainty in the measurement.

### 5.7. 2.1, 1.4, and 1.1 mm Fits With Thermal Structure

ASCA observations of A2163 suggest that the IC gas is not isothermal. We have repeated the simultaneous fits to the A2163 S-Z data for the case in which the cluster is assumed to have the ASCA determined thermal structure (Section 5.2). Using the hybrid IC gas temperature model and the consistent density model, we create models for the surface brightness of the thermal and kinematic components of the S-Z effect. For a single free parameter, we find  $v_r = +560_{-800}^{+960}$  kms $^{-1}$  and  $y_0 = 3.00 \pm .40 \times 10^{-4}$  at 68.3% confidence. These values are compared with the isothermal results in Table 3. We have repeated this analysis with the RAO differenced scans; We compare the results of the two analysis methods in Table 2 Although there is considerable uncertainty in the thermal structure of the cluster, the uncertainty it contributes to the determination of the peculiar velocity is negligible in comparison to the statistical uncertainty.

Peculiar Velocities: IC gas Temperature

Cluster	Thermal Structure	$kT_{e0}$ [keV]	$y_0 \times 10^4$	$v_r$ [kms $^{-1}$ ]
A2163	Isothermal	10.0	$3.50 \pm .47$	$+510_{-610}^{+740}$
A2163	Isothermal	12.4	$3.62 \pm .49$	$+490_{-730}^{+910}$
A2163	Isothermal	15.0	$3.70 \pm .50$	$+480_{-830}^{+1030}$
A2163	Hybrid(ASCA)	13.3	$2.96 \pm .39$	$+560_{-800}^{+960}$
A1689	Isothermal	5.0	$3.31 \pm .52$	$+190_{-350}^{+470}$
A1689	Isothermal	8.2	$3.43 \pm .59$	$+170_{-570}^{+760}$
A1689	Isothermal	10.0	$3.51 \pm .55$	$+130_{-670}^{+900}$

Table 3: Peculiar velocities assuming several values of the IC gas temperature for each cluster. For A2163, we also show the results for the Hybrid(ASCA) thermal structure. Results are for fits to the coadded data at 68% confidence.

## 6. A1689

### 6.1. X-ray Results

Abell 1689 is a distant ( $z = .181$ ) and X-ray luminous cluster of galaxies. It has been observed with the ROSAT, GINGA, and ASCA satellites. ROSAT/PSPC observations determined the peak of the X-ray surface brightness to be centered at  $13^{\text{h}} 11^{\text{m}} 29.1^{\text{s}}$ ;  $-01^{\circ} 20' 41''$  (J2000) with significant emission detected to  $8.5'$  (Daines *et al.* 1995). The X-ray surface brightness contours are nearly circular with ellipticity  $< 0.1$ . Assuming the density of the IC gas to be described by an isothermal beta model (equation 34), Daines *et al.* (1995) determine  $\theta_c = 1.13 \pm 0.12'$  and  $\beta = 0.78 \pm 0.03$  at 90% confidence. From the observed radial velocities of the cluster member galaxies, it appears there are two to three substructures superimposed along the line of sight. While this may complicate the use of this cluster to determine the Hubble constant, it has no effect on the determination of the peculiar velocity.

The presence of a cooling flow ( $\dot{M} \approx 500 M_{\odot} \text{yr}^{-1}$ ) within the central core of the cluster complicates the X-ray spectral analysis. Daines *et al.* (1995) use the combined analysis of GINGA and ROSAT spectra to determine  $T_e \sim 9$  keV outside the cooling flow. Analysis of ASCA spectra has also been used to determine the temperature of the IC gas. Assuming the gas to be isothermal outside of the central core region the

temperature is determined to be  $T_e = 8.2 \pm 1.0$  keV (Bautz *et al.* 1994).

### 6.2. 2.1 mm Observations

We observed A1689 in the 2.1 mm band on the nights of April 6, 7, and 9 1994 for a total of  $\sim 8.5$  hours. Scans were  $30'$  long with one row passing over the X-ray center and the other  $2.2'$  to the south. The RAO of the X-ray center from the start of the scan was alternated between  $12'$  and  $18'$  in sequential scans.

In Figure 9, we show the coadded  $4.6'$  and TBC scans over A1689 in Figure 9. Assuming no peculiar velocity, we fit the isothermal model for the S-Z thermal component to the coadded scans. In Figure 10, we plot the 68.3 and 95.4% confidence regions for  $y_0$  and RA. The 68.3% confidence intervals for the position and peak Comptonization are  $\Delta \text{RA} = -.01 \pm .11'$  and  $y_0 = 3.55 \pm .29 \times 10^{-4}$ . The positions of the X-ray and S-Z surface brightnesses are coincident.

Combining the peak Comptonization with the X-ray determined IC temperature, we determine the optical depth,  $\tau \sim 0.022$ . This extremely high value of optical depth is exceptional and suggests the extension of this cluster along the line of sight. The sensitivity of our measurements to cluster peculiar velocity scale linearly with  $\tau$  making this an ideal cluster for the determination of the peculiar velocity.

Fixing the position to the best fit value, we fit

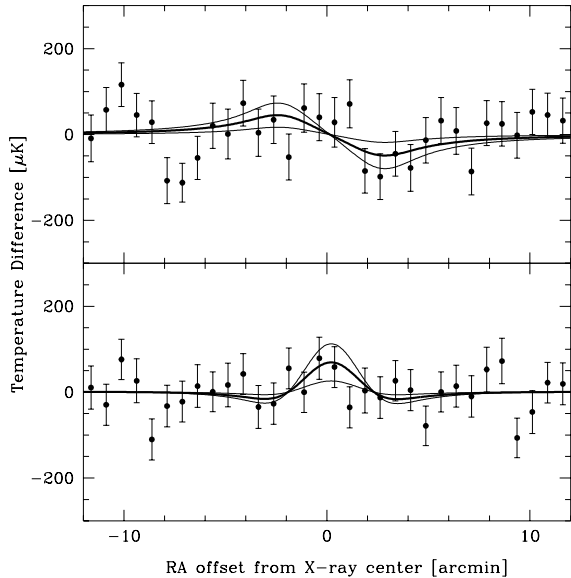


Fig. 7.— Coadded data for all May 1994 scans across A2163 at 1.4 mm. The coadded scans from the two RAOs have been offset and added to create a single coadded scan for each difference. Both the 4.6' difference (upper panel) and TBC (lower panel) are shown for the row passing directly over the peak X-ray surface brightness. The heavy line is the best fit isothermal model, and the lighter lines represent the  $1\sigma$  errors. The scans are calibrated in terms of a Rayleigh-Jeans temperature difference that completely fills one of the beams.

isothermal  $\beta$  models for the surface brightness distribution to the coadded scans. In Figure 11, We plot approximate confidence regions for  $\theta_c$  and  $\beta$ . The observed S-Z surface brightness is consistent with the best fit isothermal model parameters from the X-ray analysis and the assumption of an isothermal IC gas.

### 6.3. 1.4 mm Observations

We observed A1689 in the 1.4 mm band on the nights of May 6-9 1994 for a total of  $\sim 14$  hours. The scans were 30' long with one row passing over the X-ray center and the other 2.2' to the south. The RAO of the X-ray center from the start of the scan was alternated between 12' and 18' in sequential scans. In Figure 12, we show the coadded 4.6' and TBC scans over A1689. Fitting the data to a model for the kinematic component of the S-Z effect, we determine a

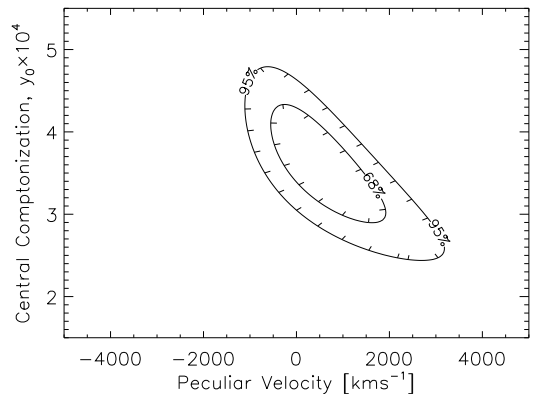


Fig. 8.— Results of fitting the 2.1, 1.4, and 1.1 mm coadded data for A2163 to isothermal ( $T_e = 12.4$  keV) source models for the two components of the S-Z effect. The 68.3% and 95.4% confidence regions in peak Comptonization and radial component of the peculiar velocity are shown.

marginally significant signal, the bulk of which is due to the residual S-Z thermal component.

### 6.4. Simultaneous Fits

We simultaneously fit isothermal ( $T_e = 8.2$  keV) models for the kinematic and thermal components of the S-Z effect to the 2.1 and 1.4 mm coadded scans. The model positions are fixed to the best fit positions from the 2.1 mm fits; the model amplitudes,  $y_0$  and  $v_r$ , are left as free parameters. In Figure 13, we plot the 68.3% and 95.4% confidence regions for  $y_0$  and  $v_r$ . The 68.3% confidence intervals for the fit parameters considered individually are  $y_0 = 3.43 \pm .59 \times 10^{-4}$  and  $v_r = +170_{-570}^{+760}$   $\text{kms}^{-1}$ . The results are unchanged for the allowed range of density model parameters. We have repeated this analysis with the RAO differenced scans; the results of the two analysis methods are compared in Table 2.

We have determined  $y_0$  and  $v_r$  assuming two other values for the isothermal IC gas temperature which exceed the range of temperatures allowed at 68.3% confidence. The peculiar velocities determined assuming  $T_e = 5$  and 10 keV are listed in Table 3. The contribution of the uncertainty in the temperature to the uncertainty in peculiar velocity ( $\Delta v_r < \pm 50 \text{ kms}^{-1}$ ) is much smaller than the statistical uncertainty in the measurement.

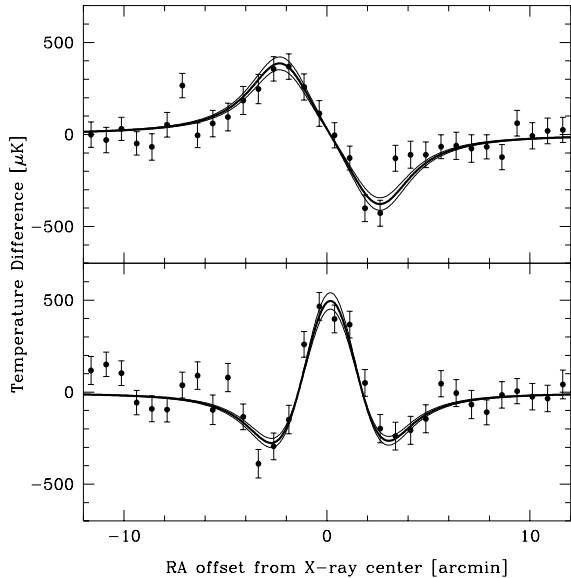


Fig. 9.— Coadded data for all April 1994 scans across A1689 at 2.1 mm. The coadded scans from the two RAOs have been offset and added to create a single coadded scan for each difference. Both the 4.6' difference (upper panel) and TBC(lower panel) data are shown for the row passing directly over the peak X-ray surface brightness. The heavy line is the best fit isothermal model, and the lighter lines represent the  $1\sigma$  errors. The scans are calibrated in terms of a Rayleigh-Jeans temperature difference that completely fills one of the beams.

## 7. Astrophysical Confusion

Although astrophysical confusion from randomly distributed sources is expected to be small at mm wavelengths (Fischer and Lange 1993), the possibility of confusion contributing a considerable systematic error to the determination of  $v_r$  in an individual cluster must be considered. In the section, we examine the contribution of confusion, including primary anisotropies of the CMB, to the uncertainty in peculiar velocity for the two clusters considered.

### 7.1. Radio Source Confusion

#### 7.1.1. A2163

A VLA search towards A2163 shows evidence of a radio source 0.8' west of the cluster center with an inverted spectrum (Herbig & Birkinshaw 1992). For

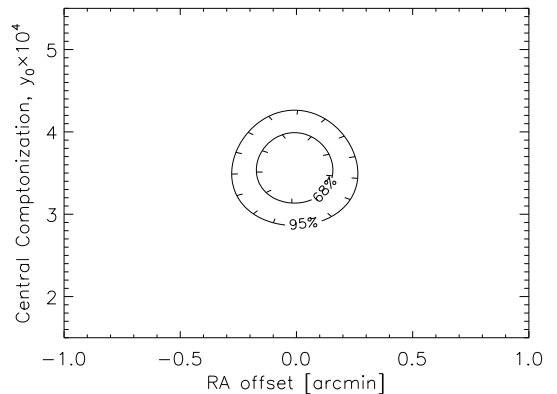


Fig. 10.— Isothermal thermal component model fit to the coadded 2.1 mm data for A1689. Assuming no peculiar velocity, the contours enclose the 68.3% and 95.4% confidence regions in peak Comptonization and RA offset from the X-ray center.

this source, the flux rises from 1 to 3 mJy between 6 and 2 cm suggesting a flux as large as 30 mJy at 2.1 mm. Recently, this cluster has been imaged with the OVRO interferometer operating at 30 GHz (Carlstrom *et al.* 1996). There is only one significant unresolved source found in the field. It is centered at  $16^{\text{h}}, 15^{\text{m}}, 43.7^{\text{s}}; -06^{\circ}, 08', 45''$  (J2000), close to the VLA source position, and has a flux of 1.4 mJy. Due to the steeply falling spectra from 2 cm to 1 cm, the source flux is likely to be less than 1 mJy in any of the SuZIE bands. However, this source is reported to be time variable (Birkinshaw 1996). Because of the elapsed time between measurements, the spectral index and the inferred fluxes in the SuZIE bands are questionable. The central region of the cluster has been imaged at 3.3 mm with the IRAM interferometer. Fischer & Radford report an upper limit of 5 mJy ( $2\sigma$  in a  $20'' \delta, 10''$  RA beam) on point source emission within 1' of the X-ray center. More sensitive observations with mm-wavelength interferometers are needed to eliminate the possibility of confusion due to this particular radio source. At present, we use the measured spectral index to infer that the flux in the SuZIE bands is likely to be less than 1 mJy.

A2163 hosts the brightest radio halo yet discovered (Herbig & Birkinshaw 1995). From measurements at 1.5 and 4.9 GHz, the integrated flux from the radio halo is estimated to be less than 1 mJy in the SuZIE 2.1 mm band (Herbig 1995). Taking the measured op-

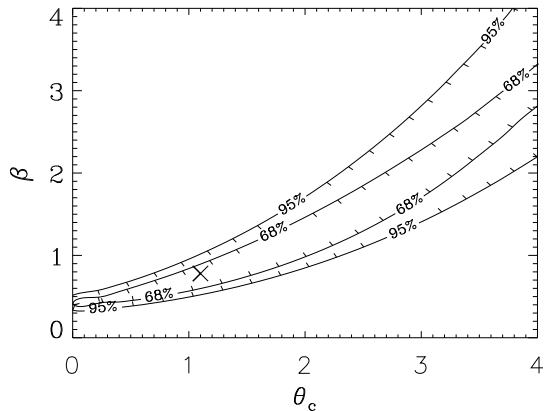


Fig. 11.— Isothermal density model parameter fits to the coadded data scans across A1689. Contours for  $\theta_c$  and  $\beta$  are shown at approximately 68% and 95% confidence. The “X” marks the best fit isothermal model parameter values from the X-ray analysis.

tical depth of A2163 and beam dilution into account, a flux of 1 mJy in any of the three observing bands corresponds to an error of  $\sim 120 \text{ kms}^{-1}$  in the derived peculiar velocity for A2163. The total uncertainty in the peculiar velocity of A2163 due to radio confusion is estimated to be  $< \pm 170 \text{ kms}^{-1}$ .

### 7.1.2. A1689

Radio emission from A1689 has been studied in detail by Slee *et al.* (1994). They find two bright sources near the cluster center which they label #13 and #15a/b. Source #13, at central position  $13^{\text{h}}, 11^{\text{m}}, 30.2^{\text{s}}; -01^{\circ}, 20', 29''$  (J2000), has a flux of 10.4 mJy and 2.75 mJy at frequencies of 1.5 GHz and 4.9 GHz. Source #15a/b, at central position  $13^{\text{h}}, 11^{\text{m}}, 31.4^{\text{s}}; -01^{\circ}, 19', 33''$  (J2000), has a flux of 41.1 mJy and 10.7 mJy at frequencies of 1.5 GHz and 4.9 GHz. Using these results, they determine the spectral indices to be  $\alpha = -1.12$  and  $\alpha = -1.14$  for sources #13 and #15a/b respectively.

Recently, sensitive maps of A1689 have been made with the OVRO interferometer operating at 30 GHz (Carlstrom *et al.* 1996). They find two significant point sources in the field with approximate positions  $13^{\text{h}}, 11^{\text{m}}, 30.3^{\text{s}}; -01^{\circ}, 20', 26''$  (J2000) and  $13^{\text{h}}, 11^{\text{m}}, 31.0^{\text{s}}; -01^{\circ}, 19', 36''$  (J2000) and fluxes 1.3 and 0.4 mJy. Within the limits of the accuracy of

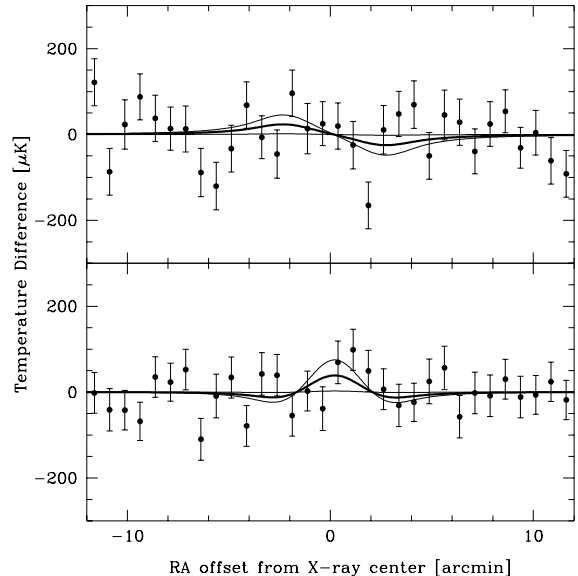


Fig. 12.— Coadded data for all April 1994 scans across A1689 at 1.4 mm. The coadded scans from the two RAOs have been offset and added to create a single coadded scan for each difference. Both the 4.6' difference (upper panel) and TBC (lower panel) data are shown for the row passing directly over the peak X-ray surface brightness. The heavy line is the best fit isothermal model, and the lighter lines represent the  $1\sigma$  errors. The scans are calibrated in terms of a Rayleigh-Jeans temperature difference that completely fills one of the beams.

the measurement ( $\sim \pm 5''$ ), these positions are coincident with the previously identified radio sources. The fluxes are used to determine the spectral indices from 4.9 to 30.0 GHz. We find  $\alpha = -1.06$  and  $\alpha = -1.14$  for sources #13 and #15a/b, demonstrating that they continue their steep decrease in flux to 30 GHz.

Using the measured spectral indices, we estimate the flux in all three SuZIE bands to be less than 0.3 mJy from the brighter of the two sources. This is especially conservative in that the brighter of the two sources is  $\approx 1'$  north of the scan path, and therefore is never inside the FWHM of any of the array beams. The smaller beam dilution and higher optical depth of A1689 means that a 1 mJy point source in each of the three SuZIE bands produces only  $\approx 63 \text{ kms}^{-1}$  error. We conclude that radio source confusion contributes  $< \pm 19 \text{ kms}^{-1}$  to the determination of the peculiar ve-

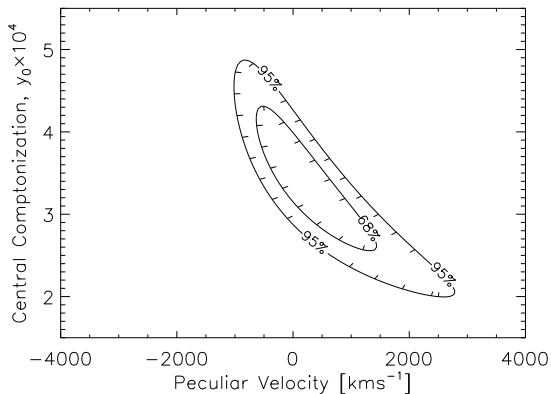


Fig. 13.— Results of isothermal ( $T_e = 8.2$  keV) model fit to correlation corrected corrected 2.1 and 1.4 mm coadded scans over A1689. The 68.3% and 95.4% confidence regions in the peak Comptonization and radial component of the peculiar velocity are shown.

locity in A1689.

## 7.2. IR Cirrus

We have used IRAS  $100\ \mu\text{m}$  sky maps to place limits on confusion due to IR cirrus emission associated with our galaxy. The images are obtained from the Infrared Sky Survey Atlas (ISSA) made available over the internet through the Infrared Processing and Analysis Center (IPAC). The images have had zodiacal light subtracted and been “de-stripped”. Each image is  $2^\circ \times 2^\circ$  centered on the peak X-ray Surface Brightness for each cluster. They are composed of  $1.5'$  square pixels, although the actual resolution of IRAS at  $100\ \mu\text{m}$  is approximately  $4' \times 5'$ .

The line of sight to A2163 passes near the edge of the galactic plane. In our scan region, the average  $100\ \mu\text{m}$  flux is  $17.2\ \text{MJy sr}^{-1}$ . The RMS variation of the flux in the  $1.5'$  square pixels across the scan is  $0.78\ \text{MJy sr}^{-1}$ . When the map is convolved with the SuZIE differential beam patterns, we find that the  $100\ \mu\text{m}$  differential flux at any point in the scan is  $< \pm 126\ \text{mJy/beam}$ . After the removal of a gradient in brightness, this result holds for fits to both the  $4.6'$  difference and the TBC. In the analysis, we have not fixed the model position to a particular point in the scan, doing this will result in a lower limit.

The line of sight to A1689 passes through a region of low IR cirrus emission. In our scan region, the average

$100\ \mu\text{m}$  flux is  $2.9\ \text{MJy sr}^{-1}$ . The RMS variation of the flux in the image  $1.5'$  square pixels is  $0.16\ \text{MJy sr}^{-1}$ . When the map is convolved with the SuZIE beam patterns, we find that the  $100\ \mu\text{m}$  differential flux at any point in the scan is  $< \pm 76\ \text{mJy/beam}$ . This result appears to be dominated by residual striping in the map. A more sophisticated analysis may result in significantly lower limits.

We scale the maps to our observing frequencies by assuming the emission in the  $100\ \mu\text{m}$  map is due entirely to 23 K dust with an emissivity,  $\epsilon \propto \nu^{-1.65}$  (Wright *et al.* 1991). In Table 4, we list the upper limits on the differential flux from IR cirrus scaled in the SuZIE bands. The flux limits are used to calculate the maximum confusion in peculiar velocity due to anisotropic dust.

Upper Limits for IR Cirrus Confusion

Cluster		Wavelength		
		2.1	1.4	1.1
A2163	Flux [mJy/beam]	0.17	0.85	1.50
	$\Delta v_{pec}$ [kms $^{-1}$ ]	20	102	180
A1689	Flux [mJy/beam]	0.10	0.51	0.93
	$\Delta v_{pec}$ [kms $^{-1}$ ]	6	32	59

Table 4: Upper limits on peculiar velocity confusion due to IR cirrus in the SuZIE bands. A1689 was observed only in the 2.1 and 1.4 mm bands.

Cluster member galaxies with slowly rising spectra could make a significant contribution to the uncertainty in peculiar velocity. Observations with existing mm-wavelength interferometers could reduce this uncertainty for a  $\tau = .01$  cluster to  $< 100\ \text{kms}^{-1}$  in a single  $1/2$  day observation.

## 7.3. Primary Anisotropies

It is also possible for the measurement of the S-Z effect to be confused by the presence of primary CMB anisotropies. The spectrum of these distortions is identical to that introduced by the S-Z kinematic effect and, therefore, especially serious for the determination of cluster peculiar velocities. The confusion in  $v_r$ , due to primary anisotropies of amplitude  $\Delta T/T$ , is  $\Delta v_r = 100 (.01/\tau) [(\Delta T/T)/3 \times 10^{-6}] \text{ kms}^{-1}$ . Haehnelt and Tegmark (1996) have estimated the confusion limits from primary anisotropies to the determination of cluster peculiar velocities. For

$\Omega = 1$  (CDM) models with  $\Omega_{baryon} = .01 - .1$ , cluster optical depth  $\tau = 0.015$ , and the SuZIE beam size, they find  $|\Delta v_{pec}| < 300 \text{ kms}^{-1}$ . This contribution to uncertainty as well as those due to foreground sources are listed for both clusters in Table 5.

Peculiar Velocities and Uncertainties		
Uncertainty	A2163	A1689
Statistical	$490^{+910}_{-730}$	$170^{+760}_{-570}$
Calibration (Flux)	$+174$ $-174$	$+5$ $-5$
Calibration (Spectral)	$+240$ $-240$	$+160$ $-160$
Baseline	$+900$ $-0$	$+140$ $-0$
IC Gas Temperature	$+20$ $-10$	$+20$ $-40$
Thermal Structure	$+70$ $-0$	$-$
Radio Confusion	$+170$ $-170$	$+19$ $-19$
IR Cirrus	$+180$ $-180$	$+32$ $-32$
Primary Anisotropies	$+300$ $-300$	$+200$ $-200$
Total	$490^{+1370}_{-880}$	$170^{+815}_{-630}$

Table 5: Peculiar velocities for A2163 and A1689 and all considered contributions to the uncertainty.

## 8. Conclusion

The kinematic S-Z effect has the potential to be a singularly sensitive probe of the peculiar velocities of distant galaxy clusters. The realization of this potential requires the separation of the thermal and kinematic components of the S-Z effect. This can only be practically carried out by observations at mm and sub-mm wavelengths. We have used observations of the S-Z effect in three mm-wavelength bands to place limits on the peculiar velocities of two distant clusters.

The cluster A2163 was observed in the 2.1, 1.4, and 1.1 mm bands. The 2.1 mm band observations are used to determine the position and morphology of the peak S-Z surface brightness. The positions of the X-ray and S-Z peak surface brightnesses are consistent when uncertainties in the ROSAT/PSPC and SuZIE pointing are included. The S-Z surface brightness is consistent with the X-ray derived density model and the assumption of an isothermal IC gas. From the 1.1 mm band observations, we report a significant detection of the S-Z thermal effect as an

increment. Simultaneously fitting the 2.1, 1.4, and 1.1 mm data with the isothermal kinematic and thermal component surface brightness models, we determine  $y_0 = 3.62 \pm .49 \times 10^{-4}$  and  $v_r = +490^{+910}_{-730} \text{ kms}^{-1}$  at 68.3% confidence. The uncertainties in  $v_r$  due to the thermal structure of the IC gas are found to be much smaller than the statistical uncertainty.

The cluster A1689 was observed in the 2.1 and 1.4 mm bands. The 2.1 mm band observations were used to determine the position of the peak S-Z surface brightness. The PSPC and S-Z peak surface brightnesses are nearly coincident. Fits to the S-Z surface brightness indicate the observed morphology is consistent with the density model determined from the X-ray observations and isothermal IC gas. Simultaneously fitting to the 2.1 and 1.4 mm data, we determine  $y_0 = 3.43 \pm .59 \times 10^{-4}$  and  $v_r = +170^{+760}_{-570} \text{ kms}^{-1}$  at 68% confidence.

Unlike the determination of  $H_0$ , the determination of cluster peculiar velocities does not place high demands on the quality of the X-ray data. The results are constant over the allowed range of X-ray derived density models. For both clusters, we have determined  $v_r$  over a broad range of X-ray temperature; the value of the peculiar velocity depends weakly on the assumed  $T_e$ . Astrophysical confusion of the peculiar velocity measurements in the two clusters is likely to be dominated by primary anisotropies of the CMB at a level  $\lesssim 300 \text{ kms}^{-1}$ . All the sources of uncertainty to the determination of cluster peculiar velocities, that we have considered, are listed in Table 5. Including uncertainties due to the uncertainty in the IC gas temperature, thermal structure, density model, calibration, and astrophysical confusion, we find  $v_r = +490^{+1370}_{-880} \text{ kms}^{-1}$  for A2163, and  $v_r = +170^{+815}_{-630} \text{ kms}^{-1}$  for A1689, both at 68% confidence.

Even though we have not yet reached sufficient sensitivity to determine individual peculiar velocities, it is possible to use results like those presented here, to probe the velocity field on very large scales. For example, Lauer & Postman (1994) (LP) report a bulk flow of galaxy clusters within a sphere of  $15,000 \text{ kms}^{-1}$  of  $v_{LP} = +730 \pm 174 \text{ kms}^{-1}$ . A2163 and A1689 lie along lines of sight separated from the direction of the LP bulk flow by only  $\approx 29^\circ$  and  $\approx 17^\circ$  respectively. If we assume that all the radial peculiar velocity of the clusters is due to a bulk flow in the direction of the LP results, we find  $v_{bulk} \approx +280^{+750}_{-550} \text{ kms}^{-1}$  at 68.3% confidence. The results of this work cannot rule out

the continuation of the LP bulk flow to  $z \sim .2$ . A modest increase in sensitivity coupled with the observation of clusters in the opposite direction to the LP flow (as a systematic check) would make a definitive test possible.

The sensitivity of the S-Z observations described here are limited by differential atmospheric emission. It should be possible to use the distinct spectral signatures of the S-Z effects to separate them from atmospheric noise. This requires simultaneous measurements along a given line of sight in at least three mm-wavelength bands. We have constructed and begun observations with an instrument capable of such measurements. This instrument should eventually have the capability of determining cluster peculiar velocities limited by the astrophysical confusion of the S-Z effect.

We would like to thank Ken Ganga for many informative discussions. The presentation has also benefited significantly from the comments of an anonymous referee. Thanks to Antony Schinkel and the entire staff of the CSO for their excellent support during the observations. The CSO is operated by the California Institute of Technology under funding from the National Science Foundation, contract #AST-93-13929. This work has been made possible by a grant from the David and Lucile Packard foundation and by a National Science Foundation grant #AST-95-03226.

## REFERENCES

- Arnaud, M., Hughes, J. P., Forman, W., and Jones, C. 1992, ApJ, 390, 345
- Bahcall, N., A., Gramann, M., and Cen, R. 1994, ApJ, 436, 23
- Bautz, M. W. *et al.* 1994, New Horizons of X-ray Astronomy - first results from ASCA, ed. Makino, F. & Ohasi, T., p. 285 Universal Academy Press, Inc. Tokyo Japan
- Birkinshaw, M., Hughes, J. P., and Arnaud, K. A. 1991, ApJ, 379, 466
- Birkinshaw, M. 1996, private communication
- Carlstrom, J. E., Grego, L., Holzapfel, W. L., and Joy M. 1996 private communication
- Cavaliere, A., Danese, L., and DeZotti, G. 1979, A&A, 75, 322
- Daines, S., Jones, C., Forman, W., and Tyson, A. 1996, preprint
- Dekel, A. 1994, ARA&A
- Elbaz, D., Arnaud, M., Bohringer, H. 1994, A&A, 293, 337
- Fischer, M. L. and Lange, A. E. 1993, ApJ, 419, 194
- Gramann, M., Bahcall, N., A., Cen, R., and Gott, R. 1995, ApJ, 441, 449
- Griffin, M. J., and Orton, G. S. 1993, Icarus, 105, 537
- Haehnelt, M. G. & Tegmark, M. 1996, MNRAS, 279, 545
- Herbig, T. & Birkinshaw, M. 1992, private communication
- Herbig, T. & Birkinshaw, M. 1995, BAAS, 26, 1403
- Herbig, T. 1995, private communication
- Holzapfel, W. L., Wilbanks, T. M., Ade, P. A. R., Church, S. E., Fischer, M. L., Mauskopf, P. D., Osgood, D. E. and Lange, A. E. 1997a, ApJ, in press
- Holzapfel, W. L., Ade, P. A. R., Church, S. E., Mauskopf, P. D., Rephaeli, Y., Wilbanks, T. M. and Lange, A. E. 1997b, ApJ, in press
- Lauer, T. R., Postman, M. 1994, ApJ, 425, 418
- Markevitch, M., Mushotzky, R., Inoue, H., Yamashita, K., Furuzawa, A., & Tawara, Y. 1996, ApJ, 456, 437
- Orton, G. S., Griffin, M. J., Ade, P., A., R., Nolt, I., G., Radostitz, J., V., Robson, E., I., and Gear, W., K. 1986, Icarus, 67, 289
- Rephaeli, Y., and Lahav, O. 1991, ApJ, 372, 21
- Rephaeli, Y. 1995a, ARA&A, 33, 541
- Rephaeli, Y. 1995b, ApJ, 445, 33
- Slee, O. B., Roy, A. L., Savage, A. 1994, Australian Journal of Physics, 47, 145
- Sunyaev, R. A. and Zel'dovich, Ya. B. 1972, Comments on Astrophysics and Space Physics, 4, 173
- Sunyaev, R. A. and Zel'dovich, Ya. B. 1980, MNRAS, 190, 413

Wright, E.L. *et al.* 1991, ApJ, 381, 200